



# Primary Head and Neck Tumour-Derived Fibroblasts Promote Lymphangiogenesis in a Lymphatic Organotypic Co-culture Model

Karina M. Lugo-Cintrón<sup>a,b,c</sup>, José M. Ayuso<sup>b,c,d</sup>, Mouhita Humayun<sup>a,b,c</sup>, Max M. Gong<sup>b,c,e</sup>, Sheena C. Kerr<sup>b,c</sup>, Suzanne M. Ponik<sup>f</sup>, Paul M. Harari<sup>g</sup>, María Virumbrales-Muñoz<sup>b,c,\*</sup>, David J. Beebe<sup>a,b,c,\*\*</sup>

<sup>a</sup> Department of Biomedical Engineering, University of Wisconsin-Madison, Madison, WI, USA

<sup>b</sup> Department of Pathology and Laboratory Medicine, University of Wisconsin School of Medicine and Public Health, Madison, WI, USA

<sup>c</sup> Carbone Cancer Center, University of Wisconsin School of Medicine and Public Health, Madison, WI, USA

<sup>d</sup> Morgridge Institute for Research, University of Wisconsin-Madison, Madison, WI, USA

<sup>e</sup> Department of Biomedical Engineering, Trine University, Angola, IN, USA

<sup>f</sup> Department of Cell and Regenerative Biology, University of Wisconsin School of Medicine and Public Health, Madison, WI, USA

<sup>g</sup> Department of Human Oncology, University of Wisconsin School of Medicine and Public Health, Madison, WI, USA

## ARTICLE INFO

### Article History:

Received 18 July 2020

Revised 5 October 2021

Accepted 5 October 2021

Available online xxx

### Keywords:

Microfluidics

Fibroblasts

Patient-Specific Model

Lymphatics

lymphangiogenesis

Head and Neck Cancer

## ABSTRACT

**Background:** In head and neck cancer, intratumour lymphatic density and tumour lymphangiogenesis have been correlated with lymphatic metastasis, making lymphangiogenesis a promising therapeutic target. However, inter-patient tumour heterogeneity makes it challenging to predict tumour progression and lymph node metastasis. Understanding the lymphangiogenic-promoting factors leading to metastasis (e.g., tumour-derived fibroblasts or TDF), would help develop strategies to improve patient outcomes.

**Methods:** A microfluidic *in vitro* model of a tubular lymphatic vessel was co-cultured with primary TDF from head and neck cancer patients to evaluate the effect of TDF on lymphangiogenesis. We assessed the length and number of lymphangiogenic sprouts and vessel permeability via microscopy and image analysis. Finally, we characterised lymphatic vessel conditioning by TDF via RT-qPCR.

**Findings:** Lymphatic vessels were conditioned by the TDF in a patient-specific manner. Specifically, the presence of TDF induced sprouting, altered vessel permeability, and increased the expression of pro-lymphangiogenic genes. Gene expression and functional responses in the fibroblast-conditioned lymphatic vessels were consistent with the patient tumour stage and lymph node status. IGF-1, upregulated among patients, was targeted to validate our personalised medicine approach. Interestingly, IGF-1 blockade was not effective across different patients.

**Interpretation:** The use of lymphatic organotypic models incorporating head and neck TDF provides insight into the pathways leading to lymphangiogenesis in each patient. This model provided a platform to test anti-angiogenic therapeutics and inform of their effectiveness for individual patients.

**Funding:** NIH R33CA225281. Wisconsin Head and Neck SPORE NIH P50DE026787. NIH R01AI34749.

© 2021 Published by Elsevier B.V. This is an open access article under the CC BY-NC-ND license (<http://creativecommons.org/licenses/by-nc-nd/4.0/>)

## 1. Introduction

Head and neck squamous cell carcinoma (HNSCC) accounts for 90% of the 65,000 head and neck cancers (HNC) diagnosed each year in the United States [1,2]. Despite ongoing research, patient outcomes

remain poor, with a 5-year survival rate of ~50%. Over 50% of HNSCC patients present diseased regional lymph node (i.e., positive lymph node status) at the time of diagnosis, which is associated with poor patient outcomes and an increased risk of developing distant metastases, leading to poor prognosis and diminished survival [3,4]. Therefore, understanding specific factors contributing to lymph node metastasis would help improve treatment strategies and, ultimately, patient outcomes. However, this is a challenging task considering the considerable heterogeneity in biological behaviour and therapeutic response of tumours from individual patients.

Tumour lymphangiogenesis (i.e., the formation of new lymphatic vessels induced by tumour-associated signalling) promotes the

\* Corresponding author: María Virumbrales-Muñoz, Wisconsin Institutes for Medical Research, University of Wisconsin. 1111, Highland Avenue, Madison, WI, US. 53705. Phone: 608-424-4156

\*\* Corresponding author: David J. Beebe, Wisconsin Institutes for Medical Research, University of Wisconsin. 1111, Highland Avenue, Madison, WI, US. 53705. Phone: 608-262-2260

E-mail addresses: [virumbralesm@wisc.edu](mailto:virumbralesm@wisc.edu) (M. Virumbrales-Muñoz), [djbeebe@wisc.edu](mailto:djbeebe@wisc.edu) (D.J. Beebe).

## Research in Context

### Evidence before this study

Head and neck cancer metastasis to lymph nodes via lymphatic vessels is a major determining factor of patient outcome, and tumour lymphangiogenesis is a known promoting factor. However, the heterogeneity of the tumour microenvironment leads to variation in inter-patient tumour characteristics and treatment response, making it challenging to predict which patients will develop tumour lymphangiogenesis. Hence, there is a clear need for predictive *in vitro* models that incorporate patient-derived components contributing to lymphangiogenesis (e.g., tumour-derived fibroblasts).

### Added value of this study

Here, we present an *in vitro* organotypic model consisting of a lymphatic vessel surrounded by primary tumour-derived fibroblasts (TDF), built for three different patients. To our knowledge, this is the first report of a head and neck cancer patient-specific microfluidic model capable of recapitulating the lymphatic-fibroblast crosstalk in the tumour microenvironment, providing biology insight for different patients.

### Implications of all the available evidence

This model offers insight into the dysregulated pathways leading to lymphangiogenesis and holds great potential for improving clinical decision-making to select personalised head and neck cancer treatments.

spread of primary tumours to regional lymph nodes [5]. Lymphangiogenesis is a multi-step process that requires the proliferation, migration, and sprouting of lymphatic endothelial cells to generate new lymphatic vessels [6]. Additionally, increased vessel permeability to large molecules is another characteristic of this process [7]. It is well known that this process is primarily driven by the vascular endothelial growth factor pathway (VEGF-C,-D/VEGFR-3) [8]. However, studies have demonstrated the involvement of other factors such as cytokines [9], matrix-metalloproteases (MMPs) [10], interstitial flow [11], extracellular matrix (ECM) [10], and changes in cellular metabolism in promoting lymphangiogenesis [12,13]. These findings raise the hypothesis that additional factors within the tumour microenvironment (TME), the niche where primary tumours develop, may be involved in promoting tumour lymphangiogenesis [14].

In HNSCC, fibroblasts are the most abundant stromal component within the TME [15]. It is also well known that fibroblasts are a key player in HNSCC metastasis, as demonstrated by several *in vitro*, *in vivo*, and pre-clinical studies showing how fibroblasts promote cancer cell proliferation and invasion progression, stemness, and metastasis [16–19]. In the context of cancer metastasis, the presence of fibroblasts has been correlated with lymphatic metastasis [20,21]. Furthermore, activated fibroblasts have been shown to secrete pro-lymphangiogenic factors [22,23]. Therefore, to improve HNSCC patient outcomes, it is important to comprehend the influence of fibroblasts in lymphangiogenesis for different patients. The use of patient-specific models could facilitate understanding of the mechanisms of lymphatic metastasis among patients and improve the selection of anti-lymphangiogenic therapies.

To unravel these mechanisms and determine personalised pharmacological targets, a model that allows the investigation of tumour-induced lymphangiogenesis within a relevant TME is needed. Current lymphatic models range from 2D/3D *in vitro* cultures to *in vivo* animal models and human subjects [24]. Conventional *in vitro* cultures offer simplicity and the amplest choice of standardised readouts but do

not incorporate physiological components (e.g., structure and cellular components). On the other hand, the dynamic nature of animal and human subjects diminishes experimental tractability as it is challenging to discriminate the contribution of specific components. Fortunately, microscale organotypic models bridge the gap between these conventional approaches as they offer the advantage of recapitulating *in vivo* 3D geometries and interactions, allowing more precise interrogation of microenvironmental conditions [25,26]. Patient-specific microscale organotypic models have emerged recently and have been leveraged to examine patient-specific gene expression alterations and responses to anti-angiogenic therapies [26–28]. Thus, we hypothesise that microscale organotypic models focused on elucidating the contribution of patient-specific TDF in lymphangiogenesis would help better understand and target head and neck cancer in a patient-specific manner.

In this paper, we developed a microfluidic organotypic model incorporating tubular lymphatic vessels and tumour-derived fibroblasts (TDF) isolated from head and neck cancer patients. This model was used to functionally investigate lymphatic vessel conditioning by HNSCC TDF and compared to human normal oral fibroblasts (HOrF). To this end, TDF were isolated from three HNSCC patients, and their lineage was verified by immunofluorescence staining and gene expression analysis. Then, TDF were embedded within a 3D matrix that surrounded a tubular lymphatic vessel, lymphatic vessels were conditioned differently by individual patient-specific TDF in our models, as evidenced by increased lymphangiogenic sprouting, permeability, and changes in gene expression. The gene expression analysis of lymphatic cells co-cultured with TDF revealed differential dysregulation of lymphangiogenic genes as compared to lymphatic cells in monoculture. Although gene profiles were unique to each patient, we found that some of the dysregulations in lymphangiogenic genes were shared across the different patients, such as upregulation of IGF-1. We validated our personalised medicine approach with an anti-IGF treatment and assessed its efficacy through functional tests such as sprout length and vessel permeability. While IGF-1 was upregulated among all patients, its blockade was ineffective at reducing vessel sprouts for all patients, and a combinational therapy approach might be needed. Overall, these results underscore the utility of our model for elucidating patient-specific mechanisms of tumour lymphangiogenesis which could help inform individual treatment decisions.

## 2. Methods

### 2.1. Head and Neck Cancer Patient Sample Processing

HNSCC diagnosis was confirmed by a pathologist for all patients. Before processing, the residual samples were maintained in transport media (DMEM basal media with gentamycin, amphotericin, and penicillin/streptomycin (Pen/Strep) at 1% v/v each). Samples were then minced and were transferred to a 15 mL conical tube containing digestion media (6 mL of transport media with 0.1% collagenase (Thermo-Fisher, 17100017), 0.1% hyaluronidase (Sigma, H3506), and 0.02% DNase (Roche, 04716728001)). The digestion mixture was incubated overnight at 37°C with rotation. To isolate cells from the sample, the sample was washed with primary HNC media (DMEM with 10% FBS, 1% penicillin-streptomycin, 1 µg/mL hydrocortisone, 10 µg/mL bovine insulin, and 50 ng/mL EGF). Then, the digested sample was filtered using a 40 µm cap filter and centrifuged at 400 g for 10 min. The cell pellet was washed twice with PBS and then cultured in primary HNC media in a T25 cm<sup>2</sup> flask. Cells were expanded into a new T75 cm<sup>2</sup> flask (Corning, CLS430641U), depending on confluency after 7–10 days. Fibroblasts were then isolated by subsequent quick trypsinizations (0.25% trypsin) at room temperature using cold trypsin, where fibroblasts detach faster than epithelial cells [29]. The

recovered fibroblasts were then cultured and expanded in a T75 cm<sup>2</sup> using fibroblast media (described in the cell culture section).

## 2.2. Cell culture

Human lymphatic endothelial cells (HLECs, ScienCell, 2500) were cultured in standard T75 cm<sup>2</sup> cell culture flasks (Corning, CLS430641U) coated with fibronectin as previously described [30,31] at a starting cell concentration of 5·10<sup>5</sup> cells. Cultures were maintained in endothelial basal medium-2 (Lonza, CC-3156) with EGM-2 MV SingleQuot Kit (Lonza, CC-4147), hereafter referred to as endothelial media. HLECs were cultured to 90-95% confluency at passage 3 for all experiments. Primary fibroblasts were routinely cultured in DMEM (Gibco, 11965092) with 10% fetal bovine serum (FBS, VWR, 97068-085), 1% Pen/Strep (ThermoFisher, 15140-122), and 1 μg/mL hydrocortisone (STEMCELL Technologies Inc., 07925). Primary human normal oral fibroblasts (HOrF, ScienCell, 2640) were cultured in standard T75 cm<sup>2</sup> cell culture flasks (Corning, CLS430641U) at a starting cell concentration of 5·10<sup>5</sup> cells in fibroblast media (ScienCell, 2301). All cultures were kept in a humidified incubator at 37°C with 5% CO<sub>2</sub>. Media was refreshed every 2-3 days, and cells were cultured to 90-95% confluency.

## 2.3. Device Fabrication

Fabrication of the PDMS microdevice was performed as previously described using standard soft lithography technique [32]. Briefly, polydimethylsiloxane (PDMS, Dow Corning, Sylgard 184) mixed 10:1 was poured over the SU-8 silicon master moulds and used to fill 25 gauge (Fisher Scientific, 14-840-84) hypodermic needles. PDMS components were then baked at 80°C for 4 h. After baking, the 280 μm PDMS rods were extracted from the needles and sandwiched between the two layers. Devices were oxygen plasma bonded to a glass-bottom MatTek dish (MatTek Corporation, P50G-1.5-30-F) and UV sterilised for 15-20 min before use.

## 2.4. Organotypic Coculture Preparation

### 2.4.1. Device preparation

All procedures in this section were performed under sterile conditions. To maximise hydrogel adhesion chamber, a two-step treatment of 2% poly(ethyleneimine) (PEI, Sigma-Aldrich, 03880) in deionised water was performed for 10 min followed by a 0.4% glutaraldehyde (GA, Sigma-Aldrich, G6257, in water) treatment for 30 min. Finally, the microdevices were washed three times with sterile deionised water.

### 2.4.2. Collagen hydrogel preparation and loading into the device

High-density rat-tail collagen type 1 (Corning, 354249, referred to as collagen through the text) was diluted with 5X PBS and neutralised with 0.5 M NaOH (Fisher Scientific, S318) for a final concentration of 1X PBS, and a pH of 7.4. A final concentration of 3 mg/mL collagen type I was achieved by adding fibrinogen (Sigma-Aldrich, F8630), fibronectin (Sigma-Aldrich, F1141) and fibroblast media. For co-culture experiments, the fibroblast media was substituted by a fibroblast cell suspension to a final concentration of 250 cells/μL (final volumes and concentrations are detailed in Table S1). After washing, 6 μL of the collagen solution was loaded through the side ports and polymerised at room temperature for 10 min. Finally, a droplet of media (5 μL) was placed on top of the side ports to prevent evaporation. Finally, devices were transferred to 37°C for 1 h to allow collagen to polymerise fully. We used a modified version of the single lumen device with a larger side port, separated from the main chamber by 3 small pillars for the indirect co-culture experiments. This design allows for patterning of a second hydrogel, with TDF at 1000 cells/μL. This increase in concentration accounts for the smaller size of the hydrogel and maintains the number of TDF constant across systems.

### 2.4.3. Lymphatic endothelial cell seeding in lumens

After incubation, a droplet of media (5 μL) was added to the input port. Then, the rod was pulled through the output port using sterilised tweezers, spontaneously filling the tubular cast with media. All fluid handling procedures were conducted with standard pipettes, leveraging the microdevice design's passive pumping mechanism to transport media through the channel [33]. HLECs were routinely trypsinised, resuspended in endothelial media at 20,000 cells/μL and seeded into the lumens (4 μL per lumen). HLEC-filled lumens were incubated at 37°C for 2 h to allow for cell attachment. Then, 10 μL of endothelial media was added per lumen, and lumens were cultured overnight at 37°C. Lumens were washed 3 times, and their media was refreshed twice daily.

For the neutralization experiments, human IGF-1 antibody (R&D Systems, AF-291-SP) and IgG isotype control (R&D Systems, AB-108-C) were prepared as per manufacturer's instructions and diluted to a final concentration of 12 μg/mL in endothelial cell media. 20 ul of neutralizing antibody solution was added per device.

## 2.5. Immunofluorescence staining and imaging in 2D and 3D

For 2D staining, fibroblasts and HLECs at passage 3 were cultured in their relevant media. Primary normal-adjacent HNSCC epithelial cells (leftover from the fibroblast isolation procedure) were cultured at passage 3 in PneumaCult™-Ex Medium (StemCell Technologies, #05008). 1000 cells/well were seeded in a glass-bottom 96 well plate (Greiner, 655086). After 48 h, cells were washed once with PBS and fixed with 4% paraformaldehyde (PFA) (Alfa-Aesar, AA433689M, in PBS) for 15 min. For 3D staining, lumens were cultured for 5 days and fixed with 4% PFA as described above.

Unless otherwise specified, all steps were performed in 2D cultures at room temperature, and cells were washed with a washing buffer (0.1% Tween 80 (Sigma-Aldrich, P1754) in PBS) in for 5 min (for 2D) and 30 min (for 3D) between every step. After cell fixation, cells were permeabilised with 0.2% Triton X-100 (MP Biomedicals, 807426) for 20 min (30 min for 3D), incubated with blocking buffer (3% Bovine Serum Albumin (BSA, Sigma-Aldrich, A9056)) and 0.1% PBS-Tween 80 (Sigma-Aldrich, P1754) for 2 h and at 4°C (overnight for 3D). Primary antibodies were diluted in staining buffer (3% BSA, Tween-80 at a final concentration of 0.2%) and incubated at 4° overnight, see table S2 for antibodies information. Secondary antibodies were diluted in staining buffer + 10% goat serum (Gibco, 16210064) to reduce unspecific binding and incubated for 2h. Texas Red-X Phalloidin (ThermoFisher Scientific, T7471) and DAPI (ThermoFisher Scientific, D3571) were added to the secondary antibody mixture to stain actin cytoskeleton and nuclei, respectively. Stained vessels were washed over two days with the washing buffer and stored in sterile PBS until imaging. Fluorescent and confocal images were using a Nikon TI® Eclipse inverted microscope (Melville, New York) and a Leica SP8 3X STED Super-resolution microscope (Wetzlar, Germany) in the UW-Madison Optical Imaging Core, respectively.

## 2.6. H&E and immunohistochemistry staining in tissue samples

Tumour tissue was formalin-fixed, embedded in paraffin, and sectioned at 5 μm. 2 colour immunohistochemistry staining was performed on the automated Ventana Discovery Ultra BioMarker Platform to identify fibroblasts. Sections were then deparaffinised with CC1 buffer (Ventana #750-500), in an EDTA-based buffer for 56 min at 95°C. Then, 300 μL of a primary antibody cocktail was added and incubated for 32 min at 37°C to label endothelial, immune, and epithelial cells (CD31, CD45, Ep-CAM information in Table S3) or reaction buffer for the negative control. Next, sections were rinsed with reaction buffer (Ventana #950-300), discovery OmniMap anti-Mouse HRP (Ventana #760-4310) for 16 min at 37°C; and ChromoMap DAB (Ventana #760-159). Sections were then treated with a discovery Inhibitor (Ventana #760-4840) to

denature/neutralise. Then, the anti-Vimentin antibody (information in Table S3), was added and incubated for 16 min at 37°C. After rinsing with reaction buffer (Ventana #950-300), discovery OmniMap anti-Mouse HRP (Ventana #760-4310) was added and incubated for 16 min at 37°C followed by another rinse step with reaction buffer and detection with the discovery purple detection kit (Ventana #760-229) for 32 min at 37°C. Sections were removed from the instrument and rinsed subsequently with: dH<sub>2</sub>O (twice), Harris hematoxylin counterstain (1:5 for 40 s), dH<sub>2</sub>O, a dehydration step, xylene, and coverslipped. Vectra™ multi-spectral imaging (Perkin Elmer) was used for image acquisition and analysis. A scanning protocol including a spectral library was created based on the ROIs and staining complexity (dual staining in a single section). The stained slides were then loaded onto the Vectra slide scanner, and 8-bit Bright Field 20X images were acquired.

### 2.7. Fibroblast proliferation assay

As per manufacturer's instructions, the proliferation of fibroblasts on 2D was tested via CyQUANT™ NF Cell Proliferation Assay (ThermoFisher Scientific, C35006). Primary fibroblasts from all patients were seeded at three densities (2,000, 5,000, and 10,000 cells per well) in a 96 well-plate and cultured for 3 days. Media was aspirated and 100 μL of the dye-binding solution was incubated at 37°C for 30 min. The fluorescence intensity was measured using a fluorescence microplate reader with excitation at ~485 nm and emission detection at ~530 nm.

### 2.8. Fluorescent image quantification

Images were processed using the National Institutes of Health ImageJ software [34]. After a rolling ball background subtraction, we projected 10 Z-planes per Z-stack. Then, sprouts were counted, and each sprout was manually traced from the lumen using the segmented line tool from which the length was measured [28].

### 2.9. Dextran diffusion assay and permeability calculation

The barrier function of the lymphatic vessel models was assessed by measuring the diffusion of 1 μM solution of Texas Red dextran (70kDa, ThermoFisher Scientific, D1830) over 15 min<sup>31</sup>. 3 μl of this solution was added to each vessel via the small port. The dextran diffusion was tracked Nikon TI® Eclipse inverted microscope (Melville, New York) equipped with a stage-top incubator (Okolab, Italy). The permeability coefficients were calculated using equation 1 [35]:

$$P = (1/I_0)[(I_f - I_0)/(t_f - t_0)](D/4), \quad (1)$$

where  $I_0$  is the total initial intensity outside the vessel,  $I_f$  is the total intensity outside the vessel at 15 min,  $t_0$  is the initial time point,  $t_f$  is the final time point of 15 min, and  $D$  is vessel diameter.

### 2.10. Verification of tumour-derived fibroblasts phenotype via qPCR

mRNA was extracted from fibroblasts seeded in a confluent 60-mm culture using Dynabeads mRNA DIRECT Purification Kit (Invitrogen, #61011) per the manufacturer's instructions and reverse transcription using iScript cDNA Synthesis kit (Bio-Rad, #170-8891). Custom qPCR primers for the interest and reference (housekeeping) genes are detailed in Table S4 and Table S5.

Finally, qPCR reactions were run using Light cycler 480 probes master mix (Roche 04887301001) in Roche's Lightcycler 480 II (Roche Molecular Systems, Indianapolis, IN). Target gene expression was normalised using the geometric mean of the reference genes GAPDH, HPRT, and PO. Relative gene expression fold changes were determined using the  $2^{-\Delta\Delta Ct}$  method compared to the reference genes. Fold changes for epithelial and fibroblast genes were calculated over

HN epithelial cells (Table S4), whereas HLECS were used for the endothelial genes (Table S5).

### 2.11. Lymphatic cell (HLEC) isolation from the device and RT-qPCR profiling of lymphatic vessels

RT-qPCR panels were used to analyse the changes in expression of multiple genes related to lymphangiogenesis in lymphatic cells after the co-culture. To selectively retrieve the lymphatic cells and the fibroblasts from the microdevice, the upper half of the microdevice was removed, exposing the collagen hydrogel. Then, the hydrogel was transferred to an Eppendorf tube containing 300 μL of 6 mg/mL collagenase type I solution (Thermo-Fisher, 17100017), and incubated for 2 min to release the cells [36]. Lymphatic cells were positively isolated from the fibroblasts using the Dynabeads® CD31 Endothelial Cell (ThermoFisher Scientific, 11155D). Then, mRNA was isolated as described in the previous section [27]. mRNA was reverse transcribed to cDNA using the RT2 Pre-AMP cDNA Synthesis Kit (Qiagen, 330451) with the RT2 Nano PreAMP Primer Mix- Angiogenesis pathway (Qiagen, 330241). cDNA was analysed by RT-qPCR using a Qiagen RT2 profiler custom panel (Qiagen, PAHS-024ZA), and data were analysed using the Qiagen online software. We used the upregulated genes identified via qPCR with GSEA to perform a gene set enrichment analysis [27]. GO term p-values were acquired and are presented as  $-\log_{10}$ .

The effectiveness of the positive selection method was assessed by staining fresh HLEC cells with calcein AM (Green, ThermoFisher Scientific, C3100MP) and fibroblasts with Calcein red/orange Calcein AM, red/orange (ThermoFisher Scientific, C34851) at 10 μM for 37°C for 15 min. After one PBS wash, 80,000 HLECs were mixed with 3,000 fibroblasts in a 1mL volume and imaged to calculate isolation efficiency.

### 2.12. Second Harmonic Imaging (SHG)

SHG images were taken on a custom-built inverted multiphoton microscope (Bruker Fluorescence Microscopy, Middleton, WI), as described previously [37]. Briefly, the system consists of a titanium: sapphire laser (Spectra-Physics, Insight DS-Dual), an inverted microscope (Nikon, Eclipse Ti), and a 40 × water immersion (1.15NA, Nikon) objective. SHG images were taken using an excitation wavelength of 890 nm, an emission bandpass filter of 440/80 nm, and a GaAsP photomultiplier tube (H7422P-40, Hamamatsu).

### 2.13. Statistics

All experiments were replicated in three independent experiments. Data were analysed using Prism 8 (GraphPad Software), and statistical significance was set at  $p < 0.05$ . Bar graphs show the mean ± standard deviation of the mean (SEM). The violin plots were generated using the kernel density method in GraphPad and show the frequency distribution of the data presented using medium smoothing. Violin plots lines show median (dashed lines) and quartiles (smaller dashed lines). One-to-one comparisons were performed with an unpaired Student t-test with Welch's correction (in case of variance inhomogeneity) after passing a Shapiro-Wilk normality test. If the normality test was failed, a non-parametric test was performed (Mann-Whitney test). Multiple comparisons were performed using one-way ANOVA with post-hoc Dunnett test. Statistical tests are specified for each experiment in the legends and corresponding text.

### 2.14. Ethics

The UWCCC Translational Science Biocore biobank provided all patient samples according to University of Wisconsin Institutional Review Board (IRB) protocol 2016-0934. Informed consent to use residual tissue was obtained prior to surgery.

2.15. Role of the funding source

The funding sources had no role in study design, the collection, analysis, and interpretation of data; in the writing of the report; and in the decision to submit the article for publication.

3. Results

3.1. Development of a lymphatic co-culture microfluidic model using HNSCC patient-derived fibroblasts

In the tumour microenvironment (TME), lymphatic vessel remodelling facilitates cancer progression and metastasis [38]. Multiple studies have reported that the surrounding stromal cells, such as

fibroblasts, create an environment that induces changes in lymphatic vessel remodelling. However, to better understand the role of tumour-derived fibroblasts (hereafter called TDF to distinguish them from fibroblasts from normal tissue) in lymphatic vessel conditioning in the context of HNSCC, we report the development of lymphatic organotypic co-culture models using HNSCC TDFs from multiple patients. To harvest HNSCC patient-derived fibroblasts, biopsy samples were collected from three HNSCC patients (Figure 1a, clinical information in Figure 5f). Tumour tissue was stained with H&E, revealing different histological patterns among patients (Fig. S1a). In addition, immunohistochemistry (IHC) staining was performed to confirm the presence of fibroblasts in the tissue of all patients (Fig. S1b). The presence of fibroblasts was confirmed (vimentin<sup>+</sup>, CD31<sup>-</sup>, Epcam<sup>-</sup>, CD45<sup>-</sup>) and their prevalence was found to vary among patients (Fig. S1c).

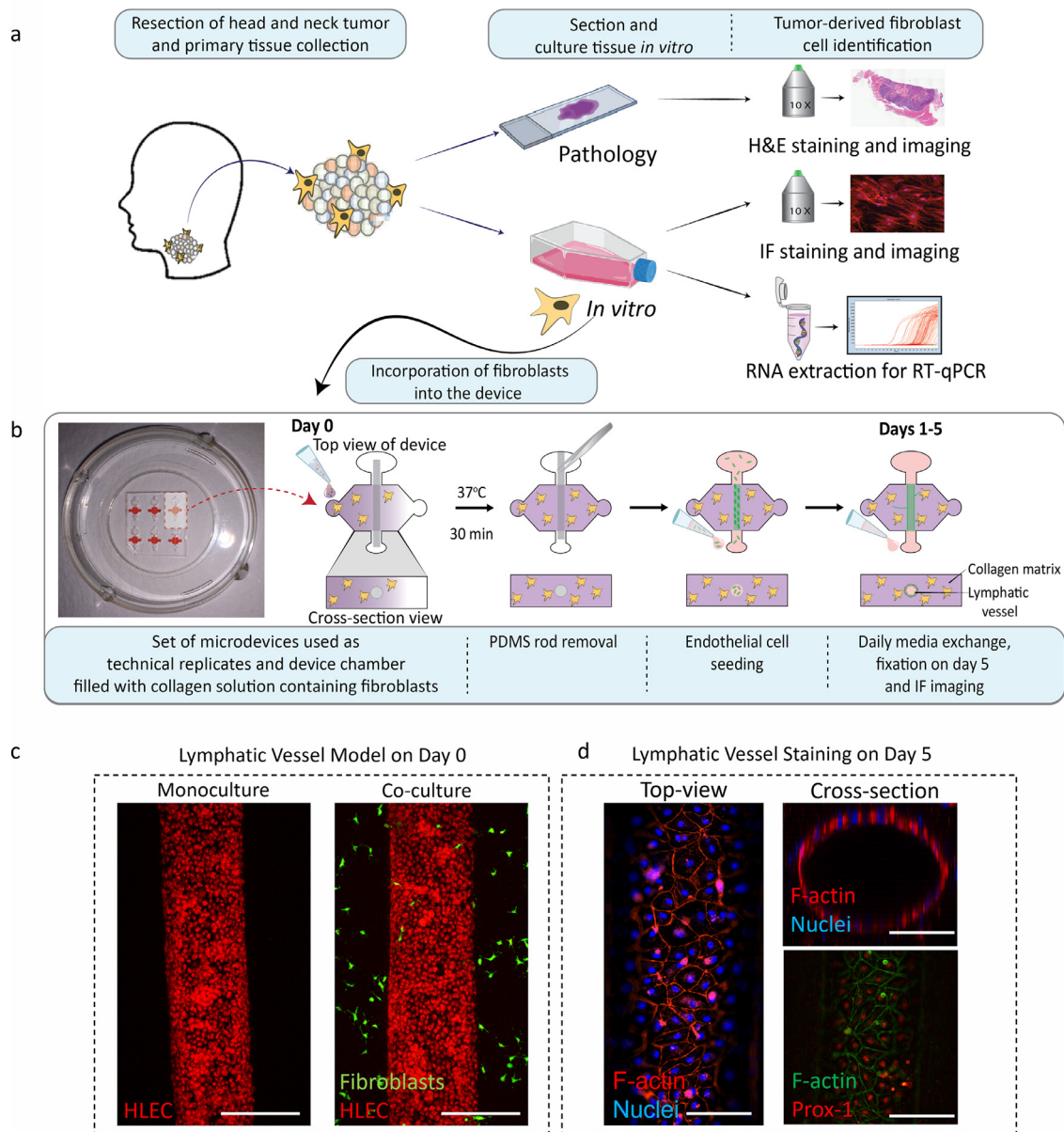


**Figure 1.** Schematic of process to obtain tumour-derived fibroblasts (TDF) from HNSCC patients and to incorporate the TDF into the lymphatic organotypic models. **a**) Schematic of the process to obtain and confirm phenotype of TDF from HNSCC patients. **b**) Microdevice picture and schematic (top- and cross-section view) showing TDFs within a collagen hydrogel on day 0. After collagen polymerization, the PDMS was removed to reveal a tubular structure that was lined with lymphatic endothelial cells (HLEC). **c-d**) Representative model staining. **c**) HLEC adhered in the lumen (red cell tracker) surrounded by HNSCC TDF (green cell tracker) from patient 1 at day 0. (Scale bar= 280 μm) **d**) Top-view of the lumen shows lumen confluency via F-actin (red) and nuclei (blue)(left) and 3D lumen structure (top-right). Prox-1 nuclear staining in red (lymphatic specific marker) and F-actin in green (bottom-right). (Scale bar= 140 μm).

Fibroblasts were isolated from the tumour tissue, and their lineage was confirmed using RT-qPCR for relevant markers (vimentin, collagen, and tenascin) and cancer-associated fibroblast markers (Fibroblast activation protein (FAP), fibroblast-specific protein-1 (FSP-1)) (Fig. S2a). TDF showed higher expression of fibroblast-specific genes (normalised to HN epithelial cells), with a significant increase in the expression of vimentin and FAP, which are canonical markers of TDF (at least 100-fold change across patients). We also disproved significant contamination with other cell types (e.g., endothelial or epithelial cells) via RT-qPCR (Fig S2b-c) and immunofluorescence (IF) (Fig S3). TDF showed a significantly lower expression of genes such as PECAM-1 and EPCAM (One-Way ANOVA and post-hoc Dunnett,  $<0.001$ ). TDF stained negative for canonical epithelial or endothelial markers (i.e., CD31 and Epcam), but did stain positive for vimentin, usually upregulated in fibroblasts. Finally, we examined the proliferation rate of the TDF via CyQUANT™ NF cell proliferation assay (Figure S4,  $p < 0.33$  via One-Way ANOVA and post-hoc Dunnett). In further experiments, we found no differences in TDF proliferation across patients at a seeding density comparable to that used in microfluidic devices. Overall, these experiments confirm the TDF lineage and purity for the isolated cells.

Following positive identification, we used our HNSCC TDF and commercial primary human lymphatic endothelial cells (HLECs) to build our lymphatic organotypic models (Figure 1b, Figure S2). The use of the same lymphatic cell population limited the variation of the model and allowed us to investigate the effects of TDF in the lymphatic vessels. For this, we adapted a recently published and validated *in vitro* model that recreates physiological aspects of the lymphatic vasculature (e.g., expression of lymphatic specific markers, leaky lumen structure, and differential protein secretion to blood vessels) [30]. Briefly, a sacrificial rod is used to cast a luminal structure within a 3 mg/mL collagen hydrogel containing tumour-derived fibroblasts in the microfluidic device (Figure 1b). After 1 h of culture, the model shows HLEC attachment into the tubular structure for the lymphatic vessel monoculture model (red cell tracker staining) (Figure 1c-left). For the co-culture model, TDF (stained with green cell tracker) are observed around the lymphatic vessel (Figure 1c-right). After 5 days, lymphatic vessels developed a confluent endothelial monolayer visualised via F-actin and nuclei staining (Figure 1d-left), defining the tubular vessel structure (Figure 1d-top right). As a further characterization, we assessed and confirmed the expression of Prospero homeobox protein 1 (PROX-1), a marker located in the nucleus of lymphatic endothelial cells, via immunofluorescence staining (Figure 1d-bottom right) [39].

### 3.2. Co-cultures with HNSCC tumour-derived fibroblasts (TDF) induce lymphatic vessel sprouting

We used the lymphatic model to evaluate the influence of TDF in tumour-induced lymphangiogenesis and vessel remodelling, which can potentially lead to HNSCC metastasis, in 3 different patient models (Figure 2a). Functional responses from co-cultures with TDF were compared to co-cultures with human oral normal fibroblasts (HORF) and lymphatic vessels monocultures at day 5 (i.e., vessel staining for imaging and sprout quantification) (Figure 2a I). For better sprout visualization, the CD31(red) staining was used for quantification, showing only the lymphatic vessels and this was used to reconstruct a 3D rendering (Figure 2 b-f).

Qualitatively, sprouts invading the matrix were visualised in the co-cultures (Figure 2c-f) but not in the monocultures (Figure 2b). Interestingly, single cell migration detached from the lumen is observed for the lymphatic monoculture, but not vessel sprouting (Figure 2b, S5). Overall, the median sprout length significantly increased in the co-cultures as compared to the HORF co-culture, and HLEC monoculture ( $p \leq 0.024$ ). HORF produced a significant increase in sprout length compared to the HLEC monoculture control

(Figures 2c & 2g). TDF from patients 1 and 2 induced significantly longer sprouts than the normal fibroblasts (Figure 2c-f & 2g), but not TDF from patient 3 (Figure 2d-f & 2g) ( $p=0.23$ , Welch-corrected t-tests to control).

Next, we quantified the number of sprouts per vessel (Figure 2h) by counting only cells stemming out of the main lumen but not single cell migration. Similar to the median sprout length, the number of sprouts significantly increased in the TDF co-cultures as compared to the HLEC monoculture control, but it was not significantly different compared to the HORF co-culture ( $16.3 \pm 3.5$ ) (Welch-corrected t-tests to control). The highest average number of sprouts was quantified in TDF co-cultures from patient 1 ( $18.0 \pm 2.5$ ) ( $p=0.003$  to HLEC). A similar number of sprouts were quantified for patients 2 and 3 ( $11.0 \pm 1.1$  and  $10.5 \pm 1.1$ , respectively) ( $p=0.0011$  and  $0.0016$ , respectively).

To elucidate if direct contact was necessary to elicit the angiogenic response, we used a modified version of the device that contained fibroblasts on a side port to enable paracrine signalling (Figure S6a). Fibroblasts were located  $800 \mu\text{m}$  away from the lumen in this modified device (Figure S6). This layout revealed a significant decrease in sprout count between paracrine signalling-only and our original monocultures and HLEC-fibroblast co-cultures ( $p < 0.0001$ ,  $p=0.092$  and  $0.0001$  for patients 1-3, respectively). A similar trend was observed for permeability ( $p > 0.94$ , one-way ANOVA and post-hoc Dunnett test) where there were no significant differences between HLEC monocultures and paracrine signalling-only co-cultures compared to the significant differences reported for our original experimental layout ( $p \leq 0.001$  for patient 1,  $p=0.002$  for patient 2, one-way ANOVA and post-hoc Dunnett test). Most cytokines are small enough to diffuse within a few minutes easily (e.g., VEGF is 38 kDa). We verified this through a diffusion experiment with 70 kDa fluorescently conjugated dextran. We added our dextran on top of the hydrogel located on the side port (i.e., where fibroblasts would be), and let it diffuse through the hydrogel. Within an hour, 50% of the dextran reached the luminal structure (Figure S8). This modified layout revealed that sprouting and permeability changes were significantly mitigated in the co-cultures when only paracrine signalling was enabled (Figure S6).

### 3.3. Co-culture with HNSCC TDF alter lymphatic vessel permeability

In addition to vessel sprout formation, lymphangiogenesis is associated with an increased permeability of the endothelium to solutes, which can facilitate metastasis [40]. Hence, we assessed the barrier function of cultured lymphatic vessels by performing a diffusion assay using 70 kDa-Texas Red dextran, which has a representative molecular weight of proteins such as serum albumin ( $\sim 67\text{kDa}$ ) (Figure 3a). The images show that the dextran was contained inside the lumen region at time 0 min in the HLEC monoculture (Figure 3b). After analysing the intensity across the lumen, it was revealed that  $\sim 20\%$  of the dextran diffused into the matrix after 15 min (Figure 3b). Using the dextran diffusion data, we calculated the permeability coefficients, including an empty lumen (cell-free collagen tubular structure) according to equation (1). Lymphatic vessel monocultures had an average permeability of  $0.8 \pm 0.2 \cdot 10^{-5}$  cm/s, a significantly lower permeability number as compared to empty lumens ( $4.6 \pm 0.6 \cdot 10^{-5}$  cm/s,  $p=0.0095$ ) (Welch-corrected t-tests to control), which confirms the barrier function of the lymphatic vessel model (Figure 3c). The co-culture with HORF did not modify the permeability of the model, whereas in the TDF co-cultures, permeability was patient-specific. Compared to the lymphatic vessel monoculture, TDF co-cultures from patients 1 and 3 had significantly higher permeability values ( $p=0.024$  and  $0.016$ , respectively), whereas patient 2 TDFs did not induce a change in permeability ( $p=0.51$ ). Taken together, these results demonstrate the ability of HNSCC TDF to alter the permeability of the lymphatic vessels in a patient-specific manner.

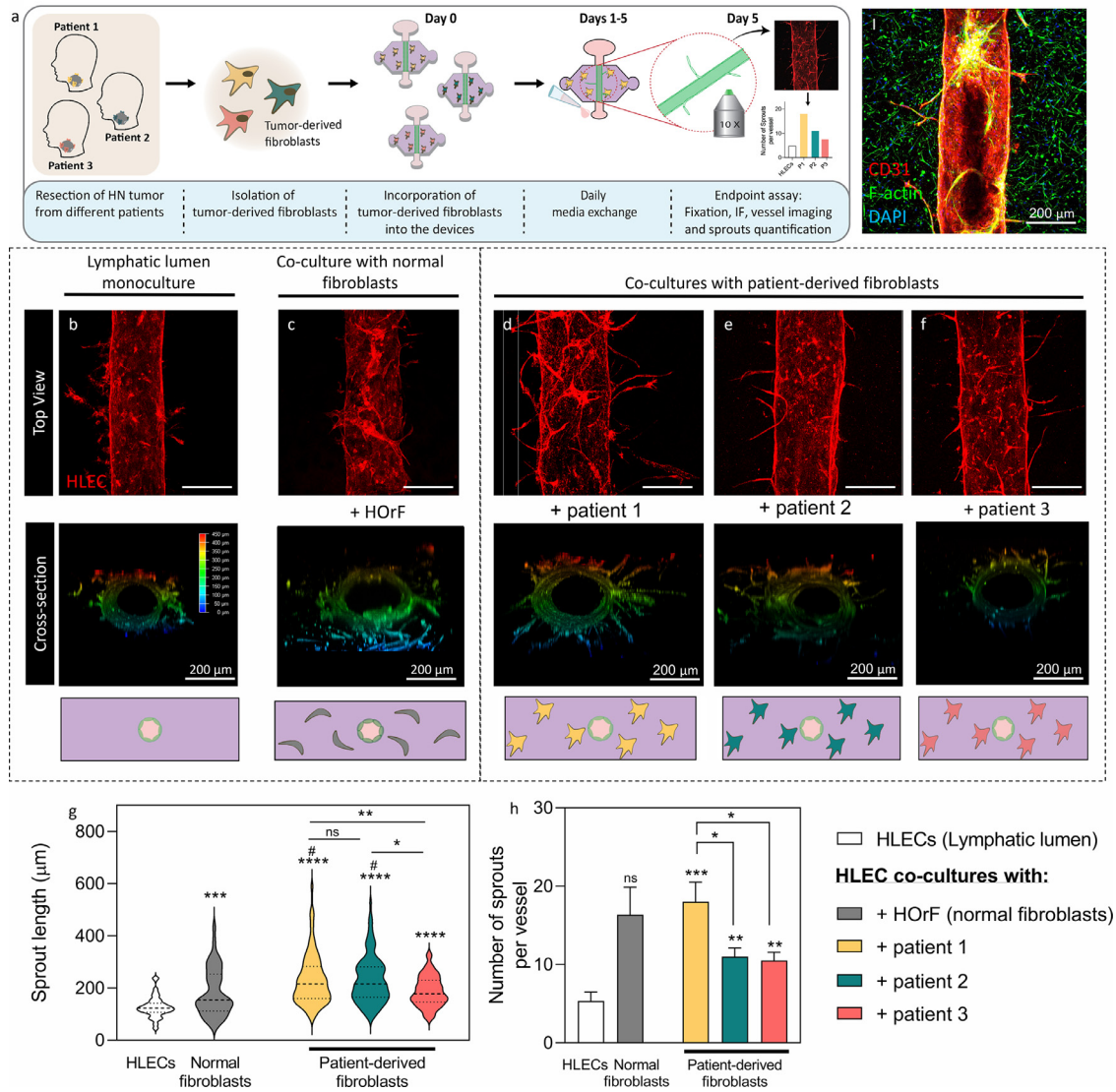


**Figure 2.** Lymphatic vessel sprouting induced by tumour-derived fibroblasts. **a)** Workflow to generate patient-specific models. **(l)** Representative top-view immunofluorescence image after 5 days of co-culture. HLECs were stained with CD31 (red), total nuclei (blue) and F-actin (green, more visible for fibroblasts). **b-f)** Top-view of the CD31 stained lymphatic vessel (Top-rows), 3D view of vessels depicting the z-position of the sprouts (middle rows) and cross-section view of the culture conditions (bottom rows). **b)** HLEC monoculture, **c)** co-culture with HORf normal fibroblasts and co-cultures with TDF from **d)** Patient 1, **e)** Patient 2 and **f)** Patient 3. **g)** Sprout length violin plot shows the distribution of the data. Dashed line represents the median. **h)** Average number of sprouts per vessel graph. (g&h) N = 4 lumens (technical replicates) each from at least 3 independent biological experiments. Bars represent average ± S.E.M. Scale bar = 280 μm \*p ≤ 0.05, \*\*p ≤ 0.01, \*\*\*p ≤ 0.001, \*\*\*\*p ≤ 0.0001, # p ≤ 0.05 compared to HORf (Welch-corrected multiple t-tests).

### 3.4. Direct co-culture with HNSCC TDF induces gene-expression changes in lymphatic vessels

Next, we sought to evaluate the effect of TDF on the lymphatic cells' gene profile. For this, we analysed HLECs from monoculture and patient-specific co-culture models via RT-qPCR for 84 genes related to angiogenesis and lymphangiogenesis (Figure 4a). After 5 days of culture, the collagen hydrogel was enzymatically degraded (Figure 4b I), and CD31<sup>+</sup> cells (HLEC) were isolated from the cell suspension (Figure 4b I-II) (>99% purity, <0.0001). HLEC vessels showed distinct gene expression profiles as compared to the co-cultures (Figure S7). A cluster analysis was performed, a technique that groups a transcriptomic profile according to their similarity, revealing that patient 1 and patient 2 were more similar to each other than to patient 3, and less closely related to the HLEC monoculture (Figure 4c and S6). We calculated the fold change of the significantly dysregulated genes for each patient (Clustergram on Figure 4c, p<0.05) (Figure 4d-f). This analysis revealed differences in the numbers of

dysregulated genes (one-way ANOVA + Dunnett post-hoc test) among patients and some shared dysregulated genes across different patients. For example, some of the upregulated pro-lymphangiogenesis genes shared among patients are insulin-like growth factor 1 (IGF1) and integrin beta 3 (ITGB3). In addition, we observed an upregulation in different lymphangiogenic genes for each patient, such as vascular endothelial growth factor-C (VEGF-C) (2.1 ± 0.4-fold change, p=0.0096) in patient 1 (Figure 4d) and KDR (VEGFR-2) (2.0 ± 0.3-fold change) in patient 2 (Figure 4e, 0.057).

For a more in-depth analysis of the profiles, we classified shared and patient-specific dysregulated genes using a Venn diagram (Figure 5a), where the upregulated genes are shown in red. From the shared genes among all patients, we identified two dysregulated genes of interest, insulin-like growth factor 1(IGF1) and integrin beta-3 (ITGB3) (Figure 5b). In TDF co-cultures from patient 1 and patient 2, IGF1 had an increase of ~6-fold change as compared to lymphatic vessel monoculture and patient 3 had a 4-fold change (Figure 5b-left). We observed the biggest fold change in TDF co-

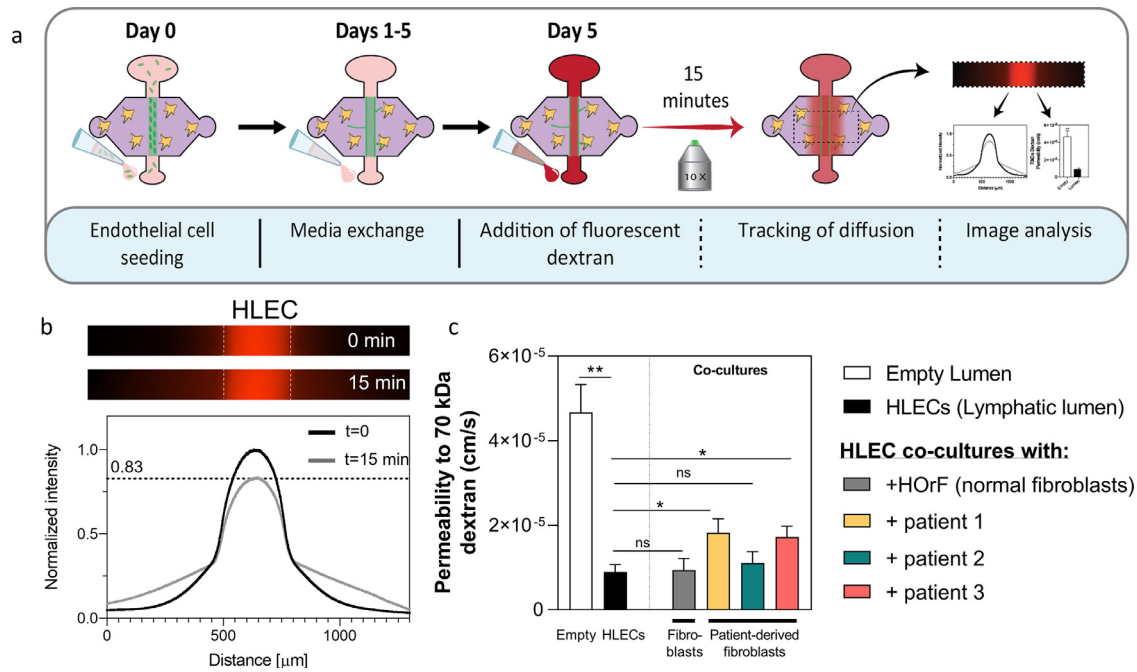


**Figure 3.** Lymphatic vessel permeability induced by tumour-derived fibroblasts. **a**) Schematic indicating the seeding procedure and the dextran diffusion assay used to generate the diffusion profile and to calculate the permeability of the vessel. **b**) Representative images of 70 kDa dextran diffusion in lymphatic monoculture (HLEC) at time 0 (top image) and at 15 min (bottom image). Diffusion profile at time 0 (black line) and at 15 min (gray line). **c**) Permeability values calculated for an empty lumen structure, lymphatic vessel monoculture (HLEC), co-culture with HoRF and co-cultures with TDF from all three patients. Comparisons were made to the lymphatic vessel monoculture. N = 4 lumens (technical replicates) each from at least 3 independent biological experiments. Bars represent average  $\pm$  S.E.M. \* $p \leq 0.05$  (Welch corrected multiple t-tests).

cultures from patient 1 (4-fold) and a similar fold change was observed in patients 2 and 3 (~1.8-fold) (Figure 5b-left). In TDF co-cultures from patients 1 and 2, metalloproteinase inhibitor 3 (TIMP3) was similarly downregulated (~0.70-fold-change), but for patient 3 it had a 0.46-fold change, lower than for patient 1 and 2 (Figure 5b-right). As for plasminogen activator inhibitor 1 (SERPINE1), all patients showed similar downregulated fold changes (~0.25 to 0.40-fold change) (Figure 5b-right).

Using the upregulated genes among patients we performed a gene ontology (GO) enrichment analysis. This bioinformatics tool relates a list of dysregulated genes to potentially dysregulated function (e.g., with an event that can be detected or observed). Thus, the GO terms define the gene product properties regarding cellular components, molecular function, and implication in biological processes (Figure 5c).

The analysis revealed GO terms related to a pro-lymphangiogenic phenotype, such as “KSHV-infection-angiogenic markers”, “Positive regulation of endothelial cell proliferation”, “Positive regulation of locomotion,” and “Transmembrane receptor protein tyrosine kinase signalling pathway”. Overall, these results confirm that all HNSCC patient-specific co-culture models have a pro-lymphangiogenic profile compared with the monoculture lymphatic model.

Next, we wondered if the dysregulated genes shared between patients explained the changes observed in the functional readouts (e.g., sprout length and permeability). For example, we observed an increase in the length of sprouts from patients 1 and 2, and we observed that patient 1 had the highest number of sprouts. One of the shared genes between patients 1 and 2 is thrombospondin-1 (THBS1), reportedly anti-lymphangiogenic [41]. Interestingly, THBS1 is similarly downregulated in patient 1 and patient 2 (Figure 5d) ( $p=0.0003$  and  $0.034$ , respectively).

Another gene shared by patients 1 and 2 is matrix-metalloproteinase-9 (MMP-9), reportedly pro-lymphangiogenic [42], and was significantly downregulated in all patients ( $p<0.0001$ ,  $p=0.0067$  and  $0.0142$ , respectively). This downregulation was significant in patients

1 and 3 (Figure 5d). Thus, these genes are consistent with the functional readouts observed in the models.

As for the functional readout of permeability, we observed the highest permeability in TDF co-cultures from patients 1 and 3. Interestingly, we found that VE-Cadherin (CDH5, a known cell-cell adhesion protein) is significantly downregulated in both patients (patients 1 and 3) (Figure 5e) ( $p=0.0094$  and  $0.016$ , respectively). VE-Cadherin downregulation corresponds to one of the first stages of angiogenesis [43,44], but fewer reports have linked it to lymphangiogenesis. Another common downregulated gene in patients 1 and 3 is the sphingosine-1-phosphate receptor 1 (S1PR1), which is implicated in the regulation of cell-to-cell interactions and has been recognised to promote lymphangiogenesis [45]. In this regard, we observe a significant downregulation of S1PR1 in patients 1 and 3 (Figure 5e). Although S1PR1 was not significantly downregulated in patient 2, the fold change was similar to patients 1 and 3 ( $p=0.0505$ ,  $0.028$  and  $0.013$ , respectively).

Taking all the data together, we showed how TDF condition lymphatic endothelial cells in a patient-specific manner to promote lymphangiogenesis and how the changes observed *in vitro* are consistent with each patient's *in vivo* pathological data (Figure 5f). Therefore, these results can be used to investigate dysregulated pathways that could be targeted to reduce lymphatic sprouting and/or permeability.

### 3.5. Functional validation of IGF1 neutralizing treatment in HNSCC TDF co-culture models

The results presented above suggest the importance of incorporating patient-specific cells into organotypic models and their potential to identify the most beneficial treatment for individual patients. For this reason, we decided to assess the validity of this approach by selecting IGF-1, a highly upregulated gene across TDF co-culture models, as a potential therapeutic target. We used the functional tests described in previous sections as readouts to evaluate the efficacy of

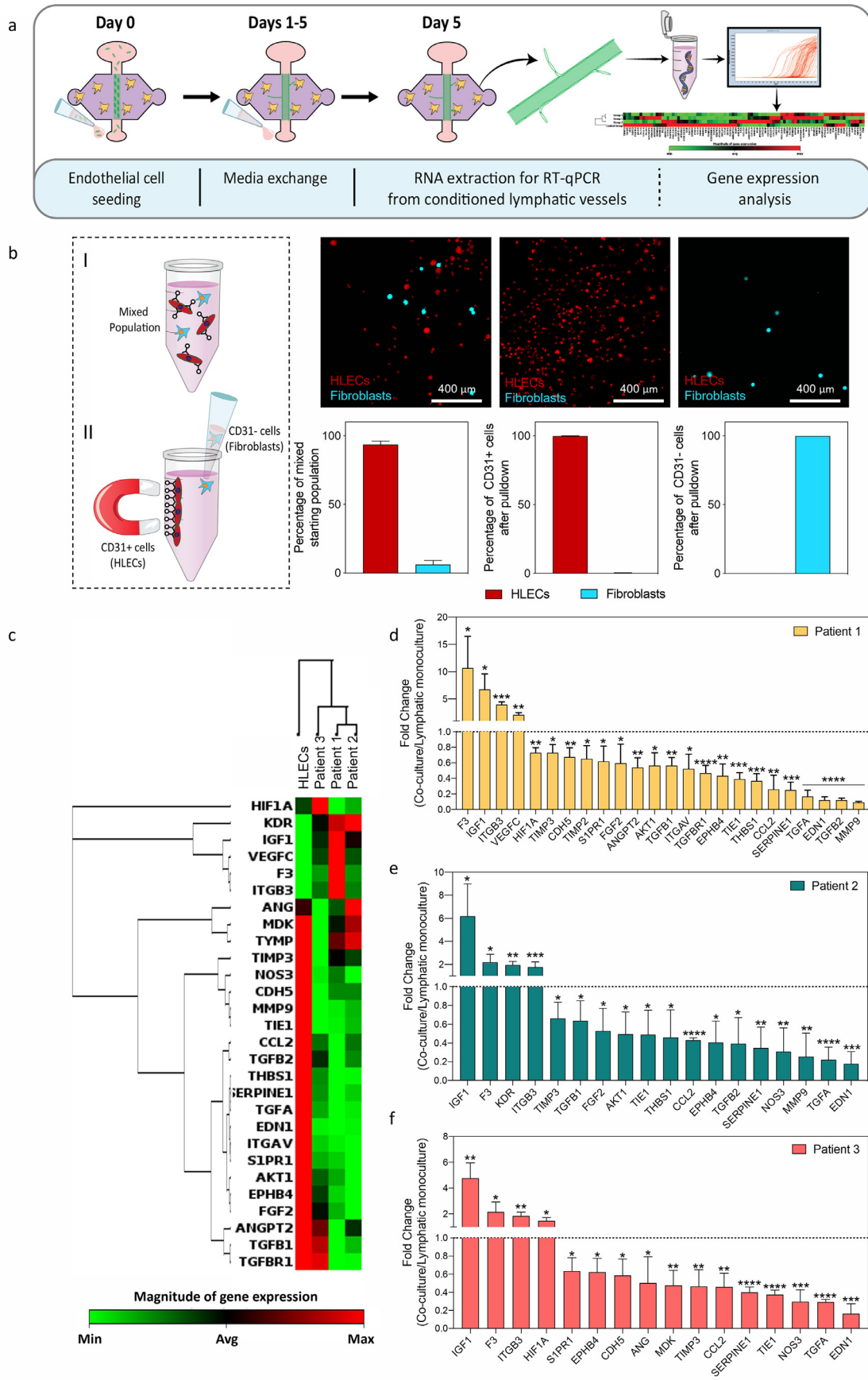


**Figure 4.** Results of qPCR analysis from the conditioned lymphatic vessels. **a)** Schematic indicating the culture procedure and the procedure to obtain mRNA from the conditioned lymphatic vessels at day 5 for gene expression analysis. **b)** Schematic of HLECs cell separation. HLECs cells attach to CD31 magnetic beads, supernatant is discarded, thus isolating

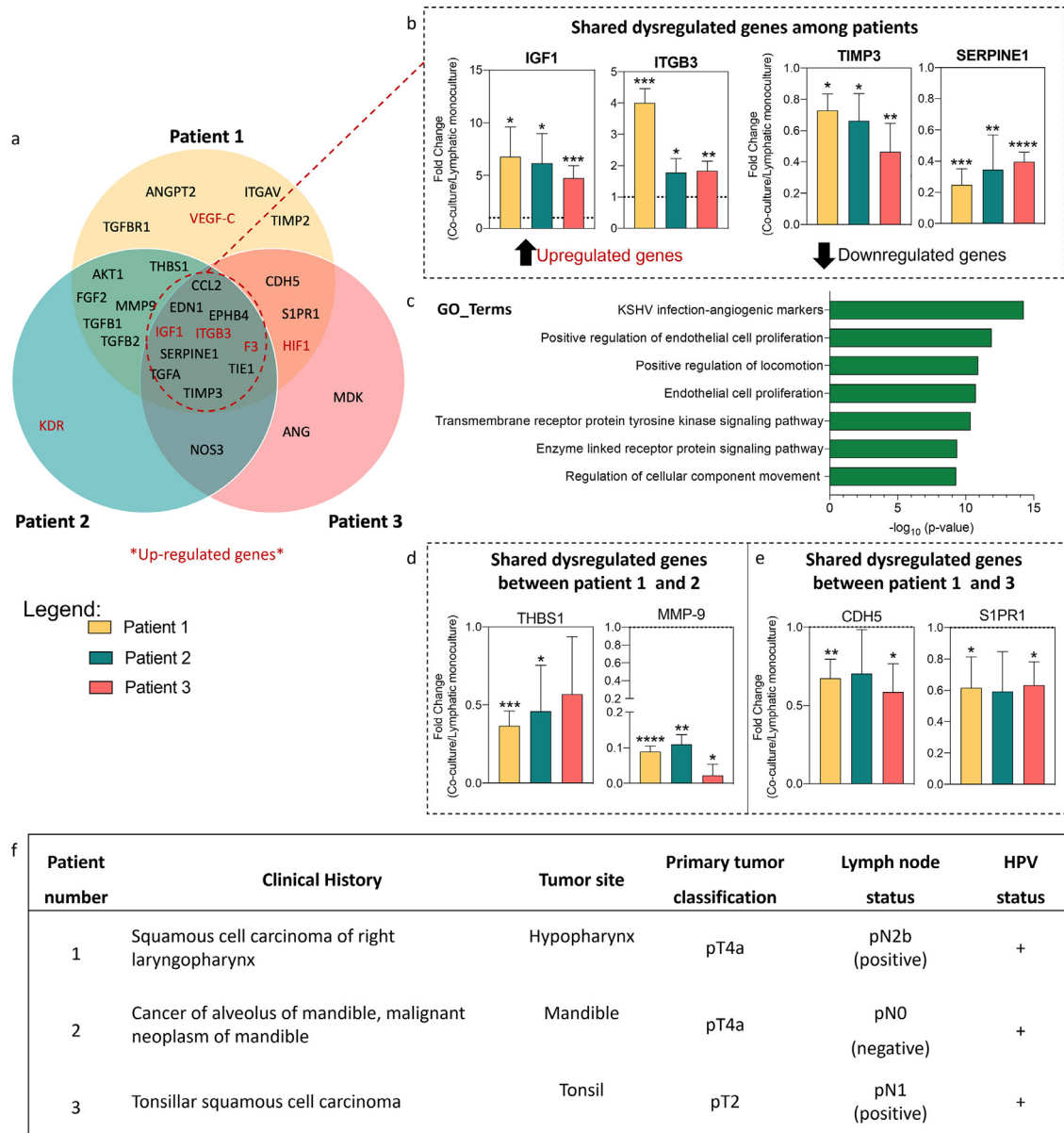


**Figure 5.** Breakdown of gene dysregulation among patients, overlaps and differences. **a)** Venn-diagram shows that some genes are shared among patients. **b)** Significant changes in gene expression (upregulated and downregulated) in all patients. **c)** Upregulated genes were used to compute expression profiles (GSEA) showed as GO terms. **d)** Significant down-regulated genes of interest in patient 1 and 2. **e)** Significant downregulated genes of interest in patient 1 and 3. **f)** Histologic subtype of head and neck squamous cell carcinoma tumours presented in this study. (b, d & e) Bars represent average  $\pm$  S.D.  $p \leq 0.05$ ,  $**p \leq 0.01$ ,  $***p \leq 0.001$ ,  $****p \leq 0.0001$  via one-way ANOVA + Dunnett post-hoc test.

anti-IGF-1 (Figure 6a). After IGF-1 treatment, vessels were visualised via CD31 staining (Figure 6b).

We observed a significant decrease in vessel sprout length for patients 2 and 3 upon treatment (0.69 and 0.86-fold change, respectively) (Figure 6c) ( $p=0.0040$ ,  $0.0012$ ,  $0.024$  via Welch-corrected t test). Interestingly, in patient 1, IGF-1 treatment significantly increased it (1.19-fold change). When assessing sprout number, we observed a similar trend for patients 2 and 3, where there was a decrease, but it was not significant (0.57 and 0.67-fold change, respectively) (Figure 6d) ( $p=0.049$ ,  $0.94$  and  $0.40$ , respectively via Mann Whitney U test).

Notably, lumens from patient 2 differed in diameter after blocking IGF-1. A slight variation in diameter is expected from the fabrication process arising from differences in the inner gauge of needles with no appreciable effect in vessel permeability or sprouting (Figure 2b-f, Figure S12,  $p=0.15$ ). However, these differences were less pronounced in control lumens, indicating that lumens increased their contractility due to the treatment (Figure 6b).

Finally, we observed a significant decrease in permeability for patient models 1 and 3 (0.21 and 0.1-fold change) (Figure 6e) following treatment, but not for patient 2 ( $p=0.012$  via Welch-corrected t-test,  $p>0.99$  and  $p<0.0001$  respectively via Mann-Whitney U-test

HLECs cells. Confocal images represent captured HLECs cells (in red) and discarded fibroblasts (in blue). The graph highlights the efficiency of HLECs cell isolation.  $N = 3$  independent biological replicates. **c)** Unsupervised clustergrams were produced using only those genes showing significant changes.  $N = 3$  independent biological experiments per patient with 4 pooled lumens each (technical replicates used to obtain enough mRNA for analysis). **d-f)** Significant changes in gene expression for each patient were plotted for patients 1, 2, and 3 to reflect the direction of the change. Bars represent average  $\pm$  S.D.  $p \leq 0.05$ ,  $**p \leq 0.01$ ,  $***p \leq 0.001$ ,  $****p \leq 0.0001$  via one-way ANOVA + Dunnett post-hoc test.

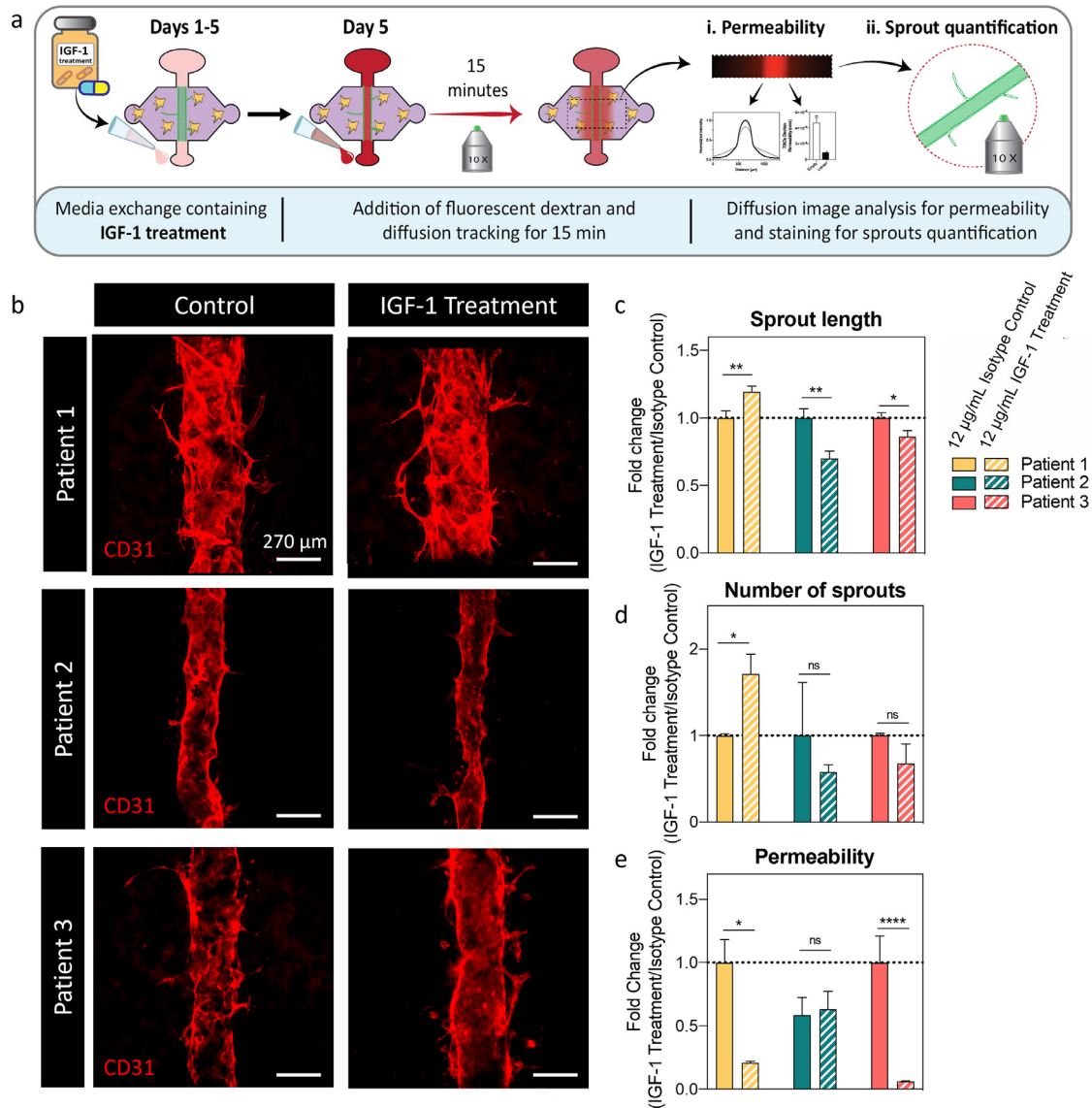


**Figure 6.** Test of IGF-1 drug identified via gene expression analysis. **a**) Schematic indicating the culture procedure for the drug testing and shows the endpoint assays (i.e., diffusion assay, permeability and sprout quantification). **b**) Representative images of control and IGF-1-treated co-culture models. 12  $\mu\text{g/mL}$  of IGF-1 treatment or IgG isotype control was added to the co-cultures. **c**) Sprout length fold change. **d**) Number of sprouts fold change. **e**) Permeability fold change (Mann-Whitney U test after normality was disproved via Kolmogorov-Smirnov test). N = 4 lumens (technical replicates) each from at least 3 independent biological experiments. Bars represent average  $\pm$  S.E.M. Scale bar = 270  $\mu\text{m}$  \* $p \leq 0.05$ , \*\* $p \leq 0.01$ , \*\*\*\* $p \leq 0.0001$  via Welch-corrected t-test unless specified otherwise.

after normality was disproved via Kolmogorov-Smirnov test). These results are consistent with our previous observations (Figure 3c). In general, these results point out that IGF-1 treatment effectively reduces vessel sprout or permeability for some patients, but it does not decrease both factors for any of the patients in this cohort. Thus, a combinational therapy based on several dysregulated genes for each patient could be a more effective therapeutic option, supporting our approach of using patient-derived cells to guide and select specific treatments for each patient.

#### 4. Discussion

Previous studies have shown that tumours can induce changes in the lymphatic vasculature (e.g., lymphangiogenesis) to increase lymph drainage [46] and promote tumour metastasis to the draining lymph nodes [47,48]. Recent lymphatic studies have focused on the interactions between cancer cells and lymphatic endothelial cells (LECs) [49–51]. However, the impact of the lymphatic-TME crosstalk on lymph node metastasis is less studied. TME components such as

fibroblasts have been identified to influence HNSCC progression profoundly and have been associated with lymphatic metastasis [17,18,52–56]. However, little is known about the mechanisms between lymphatic vessels and tumour stromal cells (e.g., TDF) that might contribute to cancer progression and lymphatic metastasis. Hence, we evaluated the influence of HNSCC TDF from individual patients on lymphatic vessel remodelling (i.e., lymphangiogenesis) that may lead to regional metastasis.

Herein, we generated organotypic models using TDF from three HNSCC patients by co-culturing them with organotypic 3D lymphatic vessels. We previously reported a detailed characterization of the HLECs, demonstrating the expression of lymphatic specific markers such as hyaluronan receptor 1 and podoplanin and the expression of endothelial markers such as CD31, VE-Cadherin, and ZO-1 [30]. Although recent groups have studied sprouting lymphangiogenesis using microfluidic platforms [57,58], to our knowledge, this is the first report studying the role of primary TDF in HNC lymphangiogenesis using an organotypic microfluidic model. We found that TDF induced a pro-lymphangiogenic response in the lymphatic vessels in

a patient-specific manner, inducing changes in lymphangiogenic sprouting and gene expression. Specifically, we found that the longest sprouts were induced in patients 1 and 2 but the highest number of sprouts in patient 1. On the other hand, HLEC vessel permeability increased in the presence of patients 1 and 3 TDF, but not for patient 2 TDF or HO rF. Importantly, the diameter of our vessels does not have a significant effect on the functional readouts used to assess the lymphangiogenic response (Figure S12).

Extracellular matrix (ECM) remodelling by the fibroblasts may be playing a role in facilitating lymphatic cell migration. To investigate if TDF present a similar behaviour in the time frame of our experiments, we used our fixed devices to perform confocal reflection microscopy, a technique that can image the collagen fibres (Figure S9)[59]. We also quantified the area occupied by the collagen fibres (per field of view) to confirm the qualitative observations that TDF co-cultures produce less robust matrices, consistent with our previous work [60]. We previously investigated the role of ECM density in the vessel function in our HLEC vessels and found that a higher collagen density induces an increase in autocrine IL-6 secretion similar to that found in an HLEC vessel - MDA-MB-231 breast cancer cell co-culture (Figure S10) [31]. The increase in IL-6 resulted in HLEC detachment and an increase in permeability (Figure S11) [30,31]. In this paper, we built upon those findings and used a lower collagen concentration to build our models to promote HLEC adhesion and decrease HLEC vessel permeability. Future studies could investigate the importance of these mechanisms in HNSCC using our model.

Finally, the changes in permeability were comparable to the monocultures, indicating a minimal angiogenic response induced by them. We believe our results highlight the inter-patient variability among the different patients. Interestingly, these changes observed *in vitro* are consistent with the *in vivo* pathological data for each patient. For example, the sprout length is consistent with the patient tumour grade (i.e., patients 1 and 2 had a higher tumour grade than patient 3) as seen in figure 5f. On the other hand, vessel permeability was consistent with the patient's lymph node status, where an increase in vessel permeability was observed in patients' 1 and 3 models, and similarly, patients' 1 and 3 had a positive lymph node status. These results suggest a relationship between tumour features and lymphangiogenic response in the models. However, a larger cohort size is needed to establish robust statistical correlations.

A limitation of this study was the use of HO rF. For standardization purposes, we used the same concentrations of HO rF as TDF. However, an abundance of fibroblasts may not necessarily be representative of a tumour-free condition. Fibroblasts are known to be active secretors of growth factors, and their presence in the tumour site is known to correlate with worse patient outcomes [20,21]. Even when we included HO rF we observed some pro-angiogenic response in the HO rF co-cultures (i.e., increase in sprout and length), the lymphatic vessel permeability did not vary. HO rF also led to sprouting, but our functional readouts revealed differences between TDF and HO rF - the angiogenic cascade did not seem to proceed toward longer sprouts with HO rF, and no changes in permeability were induced by HO rF; as opposed to TDF. Some of the TDF induced a number of sprouts comparable to HO rF, but this result is consistent with inter-patient variability of fibroblasts, in line with the results we report. Further studies should focus on elucidating the phenotype of TDF and HO rF in 3D, and how their 3D environment modifies their phenotypes and capabilities to remodel and influence the TME. Another aspect that may require further investigation is the expression of pro-angiogenic genes in HO rF, and the mechanisms underlying the differences in functional response between HO rF and TDF. Our model could be useful in investigating these differences and their relationship to lymphangiogenesis, and possible therapeutic strategies to target HNSCC fibroblasts and, in turn, improve HNSCC patient outcomes.

Interestingly, when we co-cultured TDF and lymphatic vessels only enabling paracrine signalling, we did not observe lymphatic

vessel sprouting or meaningful changes in lymphatic vessel permeability. These results validate our direct co-culture approach to mimic the *in vivo* microenvironment. Overall, these observations suggest that direct contact is necessary to induce lymphatic vessel sprouting and obtain permeability values based on the interaction between the TDF and lymphatic cells, as opposed to paracrine signalling alone. Thus, the direct co-culture setup is more beneficial to investigate the interaction between lymphatic cells and TDF than an approach merely based in paracrine signalling.

To investigate the changes observed in the functional readouts in the direct co-cultures, we performed gene expression analysis of our TDF co-cultures and lymphatic monoculture. This analysis revealed patient-specific conditioning of lymphatic vessels similar to patients 1 and 2 but less closely related to patient 3 and the HLEC monoculture. Again, this result is consistent with the tumour grade (grade IV for 1 and 2, II for 3). While RNA profiles were patient-specific, they shared some dysregulated genes. For example, some dysregulated genes shared by all patients in different magnitudes were (Insulin-like growth factor 1 (IGF1) and Integrin Subunit Beta 3 (ITGB3), which are both pro-lymphangiogenic [61–63]. The higher dysregulation shown by patient 1 suggests that IGF-1 could be a key player in the sprouting process. However, the focus of this work was the validation of our co-culture TDF models for functional testing, rather than the investigation of the crosstalk mechanisms leading to lymphangiogenesis in head and neck. Further work should investigate the importance of IGF-1 and its specificity as a therapeutic target in head and neck cancer.

Along with IGF-1, we identified other shared dysregulated genes that could account for the differences in functional readouts. Interestingly, thrombospondin-1 (THBS1), an anti-lymphangiogenic factor [41], was significantly downregulated in the patients with longest sprouts, consistent with literature reports [41,64]. As for the downregulated genes, tissue inhibitor of metalloproteinases-3 (TIMP3) and plasminogen activator inhibitor-1 (SERPINE1) have been shown to have an anti-angiogenic [65,66] and anti-lymphangiogenic role [67]. Further work using our models could elucidate their relative importance in the lymphangiogenic process.

Another interesting finding was the downregulation of VE-Cadherin (CDH5) and Sphingosine-1-Phosphate Receptor 1 (S1PR1) in patients with higher vessel permeability. These factors are involved in cell-to-cell adhesions. Thus, their downregulation could explain the vessel leakiness observed in our models [43,44,68,69]. Overall, the gene expression profiles are consistent with the functional readouts and suggest that we could target key lymphangiogenesis pathways and/or pathways associated with vessel sprouting and/or permeability changes.

As a proof of concept, we decided to test IGF-1 as a target to reduce lymphangiogenesis, given its relevance in head and neck cancer. IGF-1 has been found to induce lymphangiogenesis *in vitro* and *in vivo* [63,70], and is highly expressed in HNSCC [70,71]. Thus, blocking IGF-1 should reduce sprout length and number upon treatment. After treatment, we showed that IGF-1 treatment reduced lymphatic vessel sprouts for patients 2 and 3. Surprisingly, we observed increased vessel sprouts in patient 1, a response consistent with compensatory angiogenesis, known to happen as a resistance mechanism to anti-angiogenic therapies [72]. Although the IGF-1 treatment was not effective in reducing vessel sprouts in patient 1, it significantly reduced vessel permeability, which is another important factor in cancer metastasis. More investigation regarding the potential of IGF-1 as a therapeutic target in head and neck cancer and possible TME-elicited resistance mechanisms is needed.

Microscopy image analysis revealed a decrease in lumen diameter of P2 lumens. An explanation for that observation resides in the IGF pathway that we therapeutically blocked. It is known that IGF is implied in vessel contractility and ischemia, and therefore the effect of blocking IGF in our model could be consistent with known

molecular pathways [73–75]. This result highlights the potential of our model for functional drug testing.

Vessel permeability was significantly reduced in patient 3, yet we did not observe an increase in sprouts number and length. Thus, it is important to remember that the TDF were derived from patients at different tumour stages, thereby showing the potential of our platform to test other drugs. As an example, based on the gene expression data, we hypothesise that blocking VEGF-C might be a treatment option that would be highly beneficial to patient 1.

Here, we were interested in demonstrating the potential of functional readouts in *in vitro* models that incorporate patient-derived components contributing to lymphangiogenesis (e.g., TDF) as a tool for the precision medicine approach. Future work will require larger patient cohorts to expand and statistically correlate what we observed *in vitro* with patient response. Additionally, further mechanistic investigation of the pathways responsible for the observed functional responses would be necessary to identify actionable targets that reduce lymphangiogenesis. Finally, our model could help validate the therapeutic potential of the identified actionable targets prior to evaluating their clinical applicability.

A limitation of our study lies in the design of our setup compared with *in vivo* lymphatic function. While blood vessels act as sources for nutrients, lymphatic vessels act like “sinks”, draining waste substances. These dynamics create an interstitial flow pattern inward to the lymphatic vessel. However, our model required feeding through the vessel, thereby falling short in recapitulating this aspect of lymphatic vessels, which may, in turn, have an impact on lymphangiogenesis. Future studies should include an additional blood vessel to act as source of nutrients and generate an interstitial flow closer to an *in vivo* scenario.

Moving forward, the incorporation of cancer cells into the model would provide greater insight into the molecular mechanisms of this interaction, generating, in turn, a more complete model could lead to the identification of potential therapeutic options for each patient. As an example, the preliminary results presented here suggest the therapeutic targeting of classic anti-angiogenic agents such as sunitinib, that targets the VEGF-VEGFR2 pathway (upregulated in patients 1 and 2) could prove valuable for a subset of HNC patients, a previously reported approach for HNC model systems in combination with radiation therapy [76]. Although much of the research in vessel normalization has focused on the VEGF pathway, many essential pathways contribute to the lymphangiogenic process that may provide potential targets. This study suggests that although most patient's TDF induced a dysregulation in the VEGF pathway, each patient's fibroblasts induced dysregulations in other pathways (e.g., integrins that agents like Cilengitide could target) [77]. As other pre-clinical studies in HNC model systems have shown significant promise in predicting cancer patient outcomes [78,79], this study illustrates the potential of patient-derived lumen model systems to help guide future treatment strategies for individual cancer patients following identification of specific pathway dysregulation [27].

## Contributors

Conceptualization, K.L., M.G., J.A., S.K.; methodology, K.L., M.V., J.A., M.H., M.G.; software, M.V.; validation, K.L.; formal analysis, K.L., M.V.; investigation, K.L.; resources, D.B.; data curation, K.L., J.A., M.V.; writing—original draft preparation, K.L.; writing—review and editing, K.L., M.V., S.K., J.A., M.H., M.G., S.P., P.H., D.B.; visualization, J.A., M.H.; supervision, M.V., J.A.; project administration, K.L.; funding acquisition, P.H., D.B., M.G.. All authors have read and agreed to the published version of the manuscript.

## Data sharing

All the data generated or analysed during this study are included in this published article. All data supporting the findings in this study are also available from the corresponding authors upon Request.

## Declaration of Competing Interest

David J. Beebe holds equity in Bellbrook Labs LLC, Tasso Inc., Salus Discovery LLC, Lynx Biosciences Inc., Stacks to the Future LLC, Turba LLC, and Onexio Biosystems LLC. David J. Beebe is a consultant for Abbott Laboratories.

## Acknowledgements

We acknowledge a fellowship from the UW-Madison Graduate Engineering Research Scholars program to KML. The authors thank the University of Wisconsin Translational Research Initiatives in Pathology laboratory (TRIP), supported by the UW Department of Pathology and Laboratory Medicine, UWCCC (P30 CA014520) for use of its facilities and services.

## Supplementary materials

Supplementary material associated with this article can be found in the online version at doi:10.1016/j.ebiom.2021.103634.

## References

- [1] Cramer JD, Burtneis B, Le QT, Ferris RL. The changing therapeutic landscape of head and neck cancer. *Nature reviews Clinical oncology* 2019;16(11):669–83.
- [2] Siegel RL, Miller KD, Jemal A. Cancer statistics, 2019. *CA Cancer J Clin* 2019;69(1):7–34.
- [3] Sugiura T, Inoue Y, Matsuki R, et al. VEGF-C and VEGF-D expression is correlated with lymphatic vessel density and lymph node metastasis in oral squamous cell carcinoma: Implications for use as a prognostic marker. *International journal of oncology* 2009;34(3):673–80.
- [4] Warburton G, Nikitakis NG, Roberson P, et al. Histopathological and lymphangiogenic parameters in relation to lymph node metastasis in early stage oral squamous cell carcinoma. *J Oral Maxillofac Surg* 2007;65(3):475–84.
- [5] Mandriota SJ, Jussila L, Jeltsch M, et al. Vascular endothelial growth factor-C-mediated lymphangiogenesis promotes tumour metastasis. *EMBO J* 2001;20(4):672–82.
- [6] Karpanen T, Alitalo K. Molecular biology and pathology of lymphangiogenesis. *Annual review of pathology* 2008;3:367–97.
- [7] Nishida N, Yano H, Nishida T, Kamura T, Kojiro M. Angiogenesis in cancer. *Vasc Health Risk Manag* 2006;2(3):213–9.
- [8] Jeltsch M, Kaipainen A, Joukov V, et al. Hyperplasia of lymphatic vessels in VEGF-C transgenic mice. *Science* 1997;276(5317):1423–5.
- [9] Zheng W, Aspeltund A, Alitalo K. Lymphangiogenic factors, mechanisms, and applications. *The Journal of clinical investigation* 2014;124(3):878–87.
- [10] Vaahtomeri K, Karaman S, Makinen T, Alitalo K. Lymphangiogenesis guidance by paracrine and pericellular factors. *Genes Dev* 2017;31(16):1615–34.
- [11] Boardman KC, Swartz MA. Interstitial flow as a guide for lymphangiogenesis. *Circ Res* 2003;92(7):801–8.
- [12] Yu P, Wilhelm K, Dubrac A, et al. FGF-dependent metabolic control of vascular development. *Nature* 2017;545(7653):224–8.
- [13] Wong BW, Wang X, Zecchin A, et al. The role of fatty acid beta-oxidation in lymphangiogenesis. *Nature* 2017;542(7639):49–54.
- [14] Balkwill FR, Capasso M, Hagemann T. The tumour microenvironment at a glance. *J Cell Sci* 2012;125(23):5591–6.
- [15] Curry JM, Sprandio J, Cognetti D, et al. Tumour microenvironment in head and neck squamous cell carcinoma. *Semin Oncol* 2014;41(2):217–34.
- [16] Yu B, Wu K, Wang X, et al. Periostin secreted by cancer-associated fibroblasts promotes cancer stemness in head and neck cancer by activating protein tyrosine kinase 7. *Cell death & disease* 2018;9(11):1082.
- [17] Qin X, Yan M, Wang X, et al. Cancer-associated Fibroblast-derived IL-6 Promotes Head and Neck Cancer Progression via the Osteopontin-NF-kappa B Signalling Pathway. *Theranostics* 2018;8(4):921–40.
- [18] Qin X, Yan M, Zhang J, et al. TGFbeta3-mediated induction of Periostin facilitates head and neck cancer growth and is associated with metastasis. *Sci Rep* 2016;6:20587.
- [19] Zhou J, Wang XH, Zhao YX, et al. Cancer-Associated Fibroblasts Correlate with Tumour-Associated Macrophages Infiltration and Lymphatic Metastasis in Triple Negative Breast Cancer Patients. *J Cancer* 2018;9(24):4635–41.
- [20] Kashima H, Noma K, Ohara T, et al. Cancer-associated fibroblasts (CAFs) promote the lymph node metastasis of esophageal squamous cell carcinoma. *Int J Cancer* 2019;144(4):828–40.
- [21] Wheeler SE, Shi H, Lin F, et al. Enhancement of head and neck squamous cell carcinoma proliferation, invasion, and metastasis by tumour-associated fibroblasts in pre-clinical models. *Head Neck* 2014;36(3):385–92.
- [22] Gao P, Li C, Chang Z, Wang X, Xuan M. Carcinoma associated fibroblasts derived from oral squamous cell carcinoma promote lymphangiogenesis via c-Met/PI3K/AKT *in vitro*. *Oncol Lett* 2018;15(1):331–7.

- [23] Wei R, Lv M, Li F, et al. Human CAFs promote lymphangiogenesis in ovarian cancer via the Hh-VEGF-C signalling axis. *Oncotarget* 2017;8(40):67315–28.
- [24] Bruyere F, Noel A. Lymphangiogenesis: in vitro and in vivo models. *FASEB journal: official publication of the Federation of American Societies for Experimental Biology* 2010;24(1):8–21.
- [25] Virumbrales-Muñoz M, Ayuso JM, Gong MM, et al. Microfluidic lumen-based systems for advancing tubular organ modeling. *Chem Soc Rev* 2020;49(17):6402–42.
- [26] Ayuso JM, Park K-Y, Virumbrales-Muñoz M, Beebe DJ. Toward improved in vitro models of human cancer. *APL bioengineering* 2021;5(1):010902.
- [27] Jimenez-Torres JA, Virumbrales-Muñoz M, Sung KE, Lee MH, Abel EJ, Beebe DJ. Patient-specific organotypic blood vessels as an in vitro model for anti-angiogenic drug response testing in renal cell carcinoma. *EBioMedicine* 2019;42:408–19.
- [28] Virumbrales-Muñoz M, Chen J, Ayuso J, Lee M, Abel EJ, Beebe DJ. Organotypic primary blood vessel models of clear cell renal cell carcinoma for single-patient clinical trials. *Lab Chip* 2020;20:4420–32.
- [29] Owen JH, Graham MP, Chinn SB, et al. Novel method of cell line establishment utilizing fluorescence-activated cell sorting resulting in 6 new head and neck squamous cell carcinoma lines. *Head Neck* 2016;38(Suppl 1):E459–67.
- [30] Gong MM, Lugo-Cintrón KM, White BR, Kerr SC, Harari PM, Beebe DJ. Human organotypic lymphatic vessel model elucidates microenvironment-dependent signalling and barrier function. *Biomaterials* 2019;214:119225.
- [31] Lugo-Cintrón KM, Ayuso JM, White BR, et al. Matrix density drives 3D organotypic lymphatic vessel activation in a microfluidic model of the breast tumour microenvironment. *Lab Chip* 2020.
- [32] Jimenez-Torres JA, Peery SL, Sung KE, Beebe DJ. LumeNEXT: A Practical Method to Pattern Luminal Structures in ECM Gels. *Adv Healthc Mater* 2016;5(2):198–204.
- [33] Walker G, Beebe DJ. A passive pumping method for microfluidic devices. *Lab Chip* 2002;2(3):131–4.
- [34] Schindelin J, Arganda-Carreras I, Frise E, et al. Fiji: an open-source platform for biological-image analysis. *Nature methods* 2012;9(7):676–82.
- [35] Huxley VH, Curry FE, Adamson RH. Quantitative fluorescence microscopy on single capillaries: alpha-lactalbumin transport. *The American journal of physiology* 1987;252(1 Pt 2):H188–97.
- [36] Virumbrales-Muñoz M, Ayuso JM, Lacueva A, et al. Enabling cell recovery from 3D cell culture microfluidic devices for tumour microenvironment biomarker profiling. *Sci Rep* 2019;9(1):6199.
- [37] Ayuso JM, Gillette A, Lugo-Cintrón K, et al. Organotypic microfluidic breast cancer model reveals starvation-induced spatial-temporal metabolic adaptations. *EBioMedicine* 2018;37:144–57.
- [38] Stacker SA, Williams SP, Karnezis T, Shayan R, Fox SB, Achen MG. Lymphangiogenesis and lymphatic vessel remodelling in cancer. *Nat Rev Cancer* 2014;14(3):159–72.
- [39] Wilting J, Papoutsis M, Christ B, et al. The transcription factor Prox1 is a marker for lymphatic endothelial cells in normal and diseased human tissues. *FASEB journal: official publication of the Federation of American Societies for Experimental Biology* 2002;16(10):1271–3.
- [40] Stacker SA, Achen MG, Jussila L, Baldwin ME, Alitalo K. Lymphangiogenesis and cancer metastasis. *Nat Rev Cancer* 2002;2(8):573–83.
- [41] Cursiefen C, Maruyama K, Bock F, et al. Thrombospondin 1 inhibits inflammatory lymphangiogenesis by CD36 ligation on monocytes. *J Exp Med* 2011;208(5):1083–92.
- [42] Du HT, Du LL, Tang XL, Ge HY, Liu P. Blockade of MMP-2 and MMP-9 inhibits corneal lymphangiogenesis. *Graefes Arch Clin Exp Ophthalmol* 2017;255(8):1573–9.
- [43] Carmeliet P, Collen D. Molecular basis of angiogenesis: role of VEGF and VE-cadherin. *Annals of the New York Academy of Sciences* 2000;902(1):249–64.
- [44] Carmeliet P, Lampugnani M-G, Moons L, et al. Targeted deficiency or cytosolic truncation of the VE-cadherin gene in mice impairs VEGF-mediated endothelial survival and angiogenesis. *Cell* 1999;98(2):147–57.
- [45] Yoon CM, Hong BS, Moon HG, et al. Sphingosine-1-phosphate promotes lymphangiogenesis by stimulating S1P1/Gi/PLC/Ca2+ signalling pathways. *Blood* 2008;112(4):1129–38.
- [46] Hagendoorn J, Tong R, Fukumura D, et al. Onset of abnormal blood and lymphatic vessel function and interstitial hypertension in early stages of carcinogenesis. *Cancer Res* 2006;66(7):3360–4.
- [47] Cao R, Ji H, Feng N, et al. Collaborative interplay between FGF-2 and VEGF-C promotes lymphangiogenesis and metastasis. *Proceedings of the National Academy of Sciences* 2012;109(39):201208324.
- [48] Shayan R, Achen MG, Stacker SA. Lymphatic vessels in cancer metastasis: bridging the gaps. *Carcinogenesis* 2006;27(9):1729–38.
- [49] Lee E, Pandey NB, Popel AS. Lymphatic endothelial cells support tumour growth in breast cancer. *Sci Rep* 2014;4:5853.
- [50] Jin K, Pandey NB, Popel AS. Simultaneous blockade of IL-6 and CCL5 signalling for synergistic inhibition of triple-negative breast cancer growth and metastasis. *Breast Cancer Res* 2018;20(1):54.
- [51] Nguyen CH, Senfter D, Basilio J, et al. NF-kappaB contributes to MMP1 expression in breast cancer spheroids causing paracrine PAR1 activation and disintegrations in the lymph endothelial barrier in vitro. *Oncotarget* 2015;6(36):39262–75.
- [52] Sackett SD, Tremmel DM, Ma F, et al. Extracellular matrix scaffold and hydrogel derived from decellularised and delipidised human pancreas. *Sci Rep* 2018;8(1):10452.
- [53] Osuala KO, Sameni M, Shah S, et al. IL-6 signalling between ductal carcinoma in situ cells and carcinoma-associated fibroblasts mediates tumour cell growth and migration. *BMC Cancer* 2015;15:584.
- [54] Räsänen K, Vaehri A. Activation of fibroblasts in cancer stroma. *Experimental cell research* 2010;316(17):2713–22.
- [55] Erdogan B, Webb DJ. Cancer-associated fibroblasts modulate growth factor signalling and extracellular matrix remodelling to regulate tumour metastasis. *Biochemical Society transactions* 2017;45(1):229–36.
- [56] Orimo A, Gupta PB, Sgroi DC, et al. Stromal fibroblasts present in invasive human breast carcinomas promote tumour growth and angiogenesis through elevated SDF-1/CXCL12 secretion. *Cell* 2005;121(3):335–48.
- [57] Kim S, Chung M, Jeon NL. Three-dimensional biomimetic model to reconstitute sprouting lymphangiogenesis in vitro. *Biomaterials* 2016;78:115–28.
- [58] Osaki T, Serrano JC, Kamm RD. Cooperative Effects of Vascular Angiogenesis and Lymphangiogenesis. *Regen Eng Transl Med* 2018;4(3):120–32.
- [59] Provenzano PP, Inman DR, Eliceiri KW, et al. Collagen density promotes mammary tumour initiation and progression. *BMC medicine* 2008;6:11.
- [60] Lugo-Cintrón KM, Gong MM, Ayuso JM, et al. Breast Fibroblasts and ECM Components Modulate Breast Cancer Cell Migration Through the Secretion of MMPs in a 3D Microfluidic Co-Culture Model. *Cancers* 2020;12(5):1173.
- [61] Shigematsu S, Yamauchi K, Nakajima K, Iijima S, Aizawa T, Hashizume K. IGF-1 regulates migration and angiogenesis of human endothelial cells. *Endocr J* 1999;46(Suppl):S59–62.
- [62] Hayashi H, Sano H, Seo S, Kume T. The Foxc2 transcription factor regulates angiogenesis via induction of integrin beta3 expression. *The Journal of biological chemistry* 2008;283(35):23791–800.
- [63] Björndahl M, Cao R, Nissen LJ, et al. Insulin-like growth factors 1 and 2 induce lymphangiogenesis in vivo. *Proceedings of the National Academy of Sciences of the United States of America* 2005;102(43):15593–8.
- [64] Kaur S, Martin-Manso G, Pendrak ML, Garfield SH, Isenberg JS, Roberts DD. Thrombospondin-1 inhibits VEGF receptor-2 signalling by disrupting its association with CD47. *The Journal of biological chemistry* 2010;285(50):38923–32.
- [65] Qi JH, Ebrahem Q, Moore N, et al. A novel function for tissue inhibitor of metalloproteinases-3 (TIMP3): inhibition of angiogenesis by blockage of VEGF binding to VEGF receptor-2. *Nature medicine* 2003;9(4):407–15.
- [66] Wu J, Strawn TL, Luo M, et al. Plasminogen activator inhibitor-1 inhibits angiogenic signalling by uncoupling vascular endothelial growth factor receptor-2-alphaVbeta3 integrin cross talk. *Arterioscler Thromb Vasc Biol* 2015;35(1):111–20.
- [67] Bruyere F, Melen-Lamalle L, Blacher S, et al. Does plasminogen activator inhibitor-1 drive lymphangiogenesis? *PLoS One* 2010;5(3):e9653.
- [68] Oo ML, Thangada S, Wu MT, et al. Immunosuppressive and anti-angiogenic sphingosine 1-phosphate receptor-1 agonists induce ubiquitinylation and proteasomal degradation of the receptor. *The Journal of biological chemistry* 2007;282(12):9082–9.
- [69] Huang WC, Nagahashi M, Terracina KP, Takabe K. Emerging Role of Sphingosine-1-phosphate in Inflammation, Cancer, and Lymphangiogenesis. *Biomolecules* 2013;3(3).
- [70] Slomiany MG, Black LA, Kibbey MM, Day TA, Rosenzweig SA. IGF-1 induced vascular endothelial growth factor secretion in head and neck squamous cell carcinoma. *Biochem Biophys Res Commun* 2006;342(3):851–8.
- [71] Zhi X, Lamperska K, Golusinski P, et al. Expression levels of insulin-like growth factors 1 and 2 in head and neck squamous cell carcinoma. *Growth Horm IGF Res* 2014;24(4):137–41.
- [72] Gacche RN. Compensatory angiogenesis and tumour refractoriness. *Oncogenesis* 2015;4:e153.
- [73] Troncoso R, Ibarra C, Vicencio JM, Jaimovich E, Lavandero S. New insights into IGF-1 signalling in the heart. *Trends in Endocrinology & Metabolism* 2014;25(3):128–37.
- [74] Ungvari Z, Csizsar A. The Emerging Role of IGF-1 Deficiency in Cardiovascular Aging: Recent Advances. *The Journals of Gerontology: Series A* 2012;67A(6):599–610.
- [75] Dong F, Esberg LB, Roughead ZK, Ren J, Saari JT. Increased contractility of cardiomyocytes from copper-deficient rats is associated with upregulation of cardiac IGF-1 receptor. *American Journal of Physiology-Heart and Circulatory Physiology* 2005;289(1):H78–84.
- [76] Li J, Huang S, Armstrong EA, Fowler JF, Harari PM. Angiogenesis and radiation response modulation after vascular endothelial growth factor receptor-2 (VEGFR2) blockade. *Int J Radiat Oncol Biol Phys* 2005;62(5):1477–85.
- [77] Zhang L, Gulses A, Purcz N, Weimer J, Wiltfang J, Acil Y. A comparative assessment of the effects of integrin inhibitor cilengitide on primary culture of head and neck squamous cell carcinoma (HNSCC) and HNSCC cell lines. *Clin Transl Oncol* 2019;21(8):1052–60.
- [78] Ayuso JM, Gong MM, Skala MC, Harari PM, Beebe DJ. Human Tumour-Lymphatic Microfluidic Model Reveals Differential Conditioning of Lymphatic Vessels by Breast Cancer Cells. *Advanced Healthcare Materials* 2020:1900925.
- [79] Harari PM, Huang SM. Combining EGFR inhibitors with radiation or chemotherapy: will pre-clinical studies predict clinical results? *Int J Radiat Oncol Biol Phys* 2004;58(3):976–83.